Journal of Zhejiang University-SCIENCE A
www.jzus.zju.edu.cn; www.springer.com/journal/11582
E-mail: jzus_a@zju.edu.cn

Research Article
https://doi.org/10.1631/jzus.A2600182

High-sensitivity and robust laser-induced graphene sensing arrays for spatiotemporal pulse mapping

Guoxi LUO[1,2,4], Diying PI[1,3], Wenyan LI[1,4], Min LI[1,2,4]✉, Ping YANG[1,3], Ryutaro MAEDA[1,4], Libo ZHAO[1,2,4]✉, Zhuangde JIANG[1,2,3]

[1]*State Key Laboratory for Manufacturing Systems Engineering, State Industry-Education Integration Center for Medical Innovations, International Joint Laboratory for Micro/Nano Manufacturing and Measurement Technologies, Shaanxi Innovation Center for Special Sensing and Testing Technology in Extreme Environments, Xi'an Jiaotong University, Xi'an 710049, China*
[2]*Shandong Laboratory of Advanced Materials and Green Manufacturing at Yantai, Yantai 264000, China*
[3]*School of Mechanical Engineering, Xi'an Jiaotong University, Xi'an 710049, China*
[4]*School of Instrument Science and Technology, Xi'an Jiaotong University, Xi'an 710049, China*

Abstract: Real-time pulse monitoring could enable the diagnosis of cardiovascular conditions and thus has potential application value in cardiovascular health assessment and long-term physiological status monitoring. However, current pulse sensors are predominantly limited to point-pixel signal acquisition, which fails to emulate the 3D spatial perception inherent in traditional Chinese medicine, posing a significant challenge for subsequent diagnosis. Herein, a wearable laser-induced graphene (LIG) pulse sensor array was developed. Before fabrication of LIG, precision mechanical processing was utilized to mill an array of groove structures on the polyimide (PI) substrate to achieve stress-concentration structures, thereby enhancing sensitivity. Then, the obtained porous LIG framework was modified with MoS_2 through a dip-coating process. Unexpectedly, the MoS_2 nanosheets filled the micropores or cracks of porous LIG and mitigated cross-unit variations within the sensing array, achieving excellent batch-to-batch consistency across different sensor arrays. Furthermore, a novel chemical bond between PI and outer polydimethylsiloxane (PDMS) was developed for flexible encapsulation to prevent the adverse effects of atmospheric humidity on the functional properties of LIG and thus ensure long-term stability. The as-fabricated sensors exhibited several superior properties that are characterized by enhanced sensitivity (2.205 kPa^{-1}) in the low-pressure range (0–15 kPa), excellent consistency (maximum interdevice error of 6.61%), fast response/relaxation times (approximately 23/30 ms), high stability (over 10000 mechanical cycles), and excellent minimum detectable pressure (approximately 35 Pa). Due to the above advantages, this sensor array is applied for the detection and 3D reconstruction of pulse signals in the Cun, Guan, and Chi pulse diagnosis positions of humans. This work opens up a new avenue for wearable pulse monitoring and potential diagnosis.

Key words: Laser-induced graphene (LIG); Pulse sensor array; Mechanical milling; Chemical bonding; High consistency

1 Introduction

Over the past two decades, cardiovascular disease (CVD) has remained the leading cause of death globally (Sultana et al., 2026). Particularly in China, approximately 330 million people are affected by or have died from CVD (Zheng et al., 2025). Real-time monitoring of physiological signals can effectively diagnose diseases at an early stage, providing data support for subsequent treatment (Yang et al., 2024). As a vital physiological signal, the pulse can diagnose health conditions such as blood pressure (Li YM et al., 2025), arrhythmia (van Steijn et al., 2025), and arterial stiffness (Diana et al., 2025). Fundamentally, pulse sensors are a specialized category of micropressure transducers designed to capture the subtle pressure fluctuations on the skin surface induced by radial artery pulsations, enabling real-time physiological signal monitoring, and have been commercialized. However, traditional pulse sensors predominantly feature rigid designs with fixed shapes and hard textures, exhibiting poor skin contact. This not only potentially restricts local blood flow

✉ Min LI, limin@xjtu.edu.cn
Libo ZHAO, libozhao@xjtu.edu.cn
Guoxi LUO, https://orcid.org/0000-0003-1864-179X

Received Mar. 27, 2026; Revision accepted June 12, 2026; Crosschecked Aug. 5, 2026

and affects pulse signal generation but also limits the wearer's mobility. As such, these sensors suffer from limitations, including low measurement accuracy, significant distortion, instability, poor wearing comfort, and the inability to continuously monitor pulse signals (Yang et al., 2021; Ali et al., 2023; Chowdhury et al., 2023).

Flexible wearable sensors enable seamless, conformal integration with human skin, providing a platform for continuous, real-time monitoring of vital physiological signals and facilitation of personalized healthcare and human–machine interaction (Lu et al., 2025; Yang et al., 2025; Luo et al., 2026). In this regard, flexible devices are pivotal for the advancement of personalized pulse monitoring, offering high-fidelity data collection without compromising user comfort or mobility. Currently, wearable pulse sensors employing various sensing mechanisms have been proposed, including resistive (Zhang R et al., 2024; Zhang XK et al., 2025), piezoelectric (Tian et al., 2024; Gao et al., 2025), capacitive (Liu et al., 2024; Li X et al., 2025), and triboelectric (Wu et al., 2025; Xu et al., 2025). Although these pulse sensors can effectively detect pulse signals operating in flexible configurations, most current pulse detection devices employ single-point pulse wave sensors, which are limited to capturing one-dimensional intensity signals from a localized wrist position, failing to comprehensively reflect pulse information across the entire wrist region. From a data dimensionality perspective, such two-dimensional (2D) signals struggle to authentically simulate the spatial distribution characteristics of the "Cun, Guan, and Chi" points in traditional Chinese pulse diagnosis due to the absence of dynamic morphological features of pulse waves. Although a few instruments have attempted synchronous acquisition of the three pulse positions through multisensor measurements, the majority of existing systems still lack effective capture and reconstruction of the 3D distribution characteristics of the pulse. This restricts their application in the digitization of traditional Chinese medicine (TCM) and precision health diagnosis (Chen et al., 2021; Kang et al., 2023; Cao et al., 2025).

On the other hand, graphene, a 2D material with atomic-scale thickness, promises exceptional carrier mobility and mechanical robustness, making it an ideal candidate for flexible sensors. Remarkably, laser-induced graphene (LIG) offers a rapid, cost-effective, and mask-free fabrication route to produce highly porous 3D carbon networks, enabling the seamless integration of high-performance sensing elements onto various flexible substrates (Lin et al., 2014; Guan et al., 2025; Liu et al., 2025; Vojnović et al., 2025). Due to the above merits, LIG has been widely adopted for flexible wearable sensors (Raza et al., 2022; Mu et al., 2024; Xing et al., 2024; Hou et al., 2025; Lu et al., 2026). However, the inherent 3D porous structure of LIG results in limited sensitivity performance for fabricated mechanical sensors, especially under high loading (Wang et al., 2025). Prior studies have achieved high-sensitivity mechanical detection through material modification and structural design. However, the additional processing and structural configurations remain relatively complex (Pang et al., 2018; Chhetry et al., 2019; Zhao et al., 2021; Huang et al., 2024). In addition, this 3D microstructural disorder of LIG directly translates into electrical property dispersion, manifesting as nonreproducible initial resistances and piezoresistive response curves across different sensors, thus resulting in poor performance consistency for LIG-based sensors (van Volkenburg et al., 2023). Simultaneously, due to the enormous specific surface area, abundant nanopores, and numerous hydrophilic oxygen-containing functional groups, LIG can readily trap water molecules from the environment through physical adsorption and capillary condensation (Fei et al., 2023). As such, the absorption and desorption of water molecules introduce additional hysteresis effects and may induce expansion stresses in the microstructure to degrade the stability of the prepared device. These factors have severely affected the electromechanical properties and in turn significantly reduced the stability and long-term reliability of LIG-based sensors.

Herein, to address the requirement for 3D pulse monitoring, a high-sensitivity and robust LIG sensing array was developed. Initially, specific grooved structures were fabricated on the polyimide (PI) substrate via mature and straightforward precision mechanical milling to enhance sensitivity by leveraging stress concentration. The geometric parameters of these grooves were optimized through finite element analysis (FEA). Then, the LIG sensing arrays were patterned onto the PI substrate using an optimized laser scribing process. Subsequently, MoS_2 solution was used to modify the 3D porous graphene to eliminate microstructural disorder and thus enhance the consistency of the electromechanical response among different sensors. Afterwards, a facile and high-strength chemical bonding process was developed to encapsulate LIG sensor arrays with a polydimethylsiloxane (PDMS) cover film at room temperature, which endows the device with good sealing properties to counteract moisture absorption and thereby promises excellent stability. Finally, a dedicated system encompassing detection circuitry and a mobile-based user interface was developed to reconstruct the acquired pulse signals into 3D signals. This work provides significant insights and a valuable reference for effective pulse monitoring and promises a potential realization of the digitization of TCM.

2 Experimental

2.1 Materials

PI film was purchased from Alfa Aesar (China). PDMS film was purchased from Hangzhou Westru Technology Co. Ltd. (China). MoS_2 was obtained from Jiangsu XFNANO Company (China). 3-Mercaptopropyl trimethoxysilane (MPTMS) was purchased from TCI Development Co., Ltd. (China). All materials were used as received without further purification.

2.2 Flexible printed circuit and precision mechanical milling on the PI substrate

Flexible printed circuit (FPC) technology was employed to fabricate copper electrode wires with a thickness of 18 μm on the initial PI substrate surface. Precision mechanical milling was utilized to create a certain number of square grooves on the 1.2 mm×1.2 mm FPC PI substrate, with a milling cutter diameter of 0.5 mm and a spindle speed of 9000 r/min.

2.3 Design and optimization of structural parameters of machined grooves

Numerical simulation of the sensitive layer's deformation under external force was performed using the FEA software COMSOL. A 3D model with actual structural dimensions was established and meshed using tetrahedral elements (C4D4). Boundary loads were applied to the model with fixed constraints added. Vertical pressures of equal magnitude were applied to the model under different structural parameters, including the number, depth, and length of grooves, and the resulting strain values were calculated. Under environmental conditions, the final device was fabricated based on the optimized structural parameters.

2.4 Fabrication of LIG sensing array

To prepare the sensitive layer, the FPC PI substrate was cleaned and then dried by baking on a hot plate at 100 °C for 10 min. Subsequently, a CO_2 infrared laser (VLS2.30, Universal Laser Systems, the USA) was used to etch the microchannel-structured PI film (250 μm) in ambient air, creating an LIG 3D porous structure. A 10.6 μm CO_2 laser with a maximum power of 30 W was employed for laser scribing at 1000 pulses per inch (1 inch=2.54 cm) under varying power and speed conditions. The laser scribing parameters, specifically power and scan rate, were thoroughly investigated and optimized to ensure high-quality LIG formation. Following the established laser induction parameters, a uniformly spaced five-strip LIG sensing array was integrated onto the FPC PI substrate along the preprocessed electrodes.

Following laser-etch fabrication, the LIG was decorated with MoS_2 solution through a dip-coating process. At room temperature, a 1:1 volume ratio mixture of 100 mL *N*-methyl-2-pyridone and deionized water was prepared. This solution was added to 40 mg MoS_2 powder and vigorously sonicated for 90 min to achieve uniform dispersion. The prepared PI substrate was immersed in the MoS_2 solution and sonicated for 30 s using an ultrasonic power of 60 W. The sample was then removed from the solution and dried on a hot plate at 100 °C for 10 min, yielding MoS_2-decorated LIG.

2.5 Bonding process between PI and PDMS

At room temperature, the PI surface was treated with a 2% (volume fraction) MPTMS aqueous solution for 2 s to induce hydrolysis and nucleophilic reactions. The sample was then immediately rinsed with distilled water and air-dried. Subsequently, the bonding faces of the PI substrate and PDMS film were subjected to plasma treatment (radio frequency power 100 W, 120 s). The surfaces were immediately bonded together for 10 min after oxidation to achieve irreversible bonding at room temperature. Due to the high reactivity of the thiol-terminated silane coupling agent, the solution was prepared fresh for each experiment and discarded after approximately 30 min.

2.6 Characterization and measurements

The surface morphology of LIG and MoS_2-decorated LIG was investigated using scanning electron microscopy (SEM, Sigma 360, ZEISS, Germany). Characteristic elements in PI films before and after laser ablation were analyzed using X-ray photoelectron spectroscopy (XPS, Scientific K-Alpha, Thermo, the USA). The structural composition of LIG was analyzed using Raman spectroscopy (Raman, LabRAM HR Evolution, Horiba, Japan). Shear strength testing was conducted using a mechanical tensile tester (PLD-5) to evaluate the bond strength between PI and PDMS films.

The performance of the LIG sensing array was evaluated using a dedicated experimental test platform. A signal generator produced an electrical signal amplified by a power amplifier, which directly drove a vibrator to generate periodic vibrations. The magnitude of force applied to the LIG sensor was measured via the force sensor. By recording the current pressure signal, the current output and voltage output of the LIG sensor under that pressure could be measured.

3 Results and discussion

3.1 Sensing mechanism and structural design

The heart, as the driving force of the human circulatory system, periodically propels blood through arteries and veins to complete the pumping and circulation process. The generated pulse waves contain rich cardiovascular physiological information, from which key physiological characteristics such as the pulse wave (P-wave), tidal wave (T-wave), and bifurcated wave (D-wave) can be extracted. For example, in TCM pulse palpation, practitioners place their fingertips in three distinct positions: Cun, Guan, and Chi. Since the human fingertip functions as a highly sensitive 3D force sensing unit, the diagnostic data acquired by one fingertip are essentially spatiotemporal 3D signals. To emulate the TCM pulse palpation process, the developed wearable sensor must function as a highly sensitive subtle pressure transducer. Furthermore, to capture spatiotemporal 3D signals, a single pulse sensor should be engineered as a sensing element array. Arranged along the direction of blood flow, this configuration enables the detection and reconstruction of 3D pressure signals at the acupoint interface, as shown in Fig. 1a.

Fig. 1b shows the schematic layout of the developed sensor array, featuring an ultrathin bilayer structure: the bottom flexible substrate consists of a 250 μm thick PI film with microgroove structures. This substrate offers excellent flexibility and mechanical strength, providing a stable support structure while maintaining good physical integrity under various complex usage scenarios. To facilitate subsequent performance testing, copper conductors (200 μm in width) were fabricated on the PI film for signal extraction. Additionally, a stress-concentrating structure was created by grooving the PI film substrate through a mechanical milling process. The graphene prepared by laser etching serves as the core sensing element, designed in a rectangular pattern size of 1.4 mm×8 mm. The top cover consists of a flexible PDMS membrane of 50 μm, effectively shielding the graphene sensing layer from external influences. The top cover and substrate were assembled together through our previously reported chemical bonding process (Luo et al., 2025) to form the encapsulation structure of the sensor.

To enhance the sensing sensitivity, a microgroove structure was designed, and the influences of dimensions on pressure sensing performance were investigated. Using COMSOL FEA software, a 3D model with actual dimensions was created. Through FEA simulation, the deformation of the sensitive layer under external pressure was modeled to obtain its strain curve and thereby determine the actual resistance change of the sensitive layer. Fig. 1c displays the model's deformation under 100 kPa pressure. Theoretically, higher average strain levels correlate with increased pressure sensor sensitivity. By simulating the impact of various structural parameters on sensor performance, critical design parameters were identified and optimized. First, the effect of the microgroove structure count (n) on the sensor performance was examined. Simulations were conducted with microgroove counts of 1, 2, 3, and 4, as shown in Fig. 1d. The strain level in the sensitive layer increases with the number of stress-concentrating structures. However, due to material dimensional constraints and scale requirements for milling, the optimal number of microgroove structures was ultimately determined to be 3. Subsequently, the depth (d) of the microgroove structures was also investigated, as shown in Fig. 1e. As the depth increased from 20 to 50 μm, it was observed that the stress on the surface gradually increased with

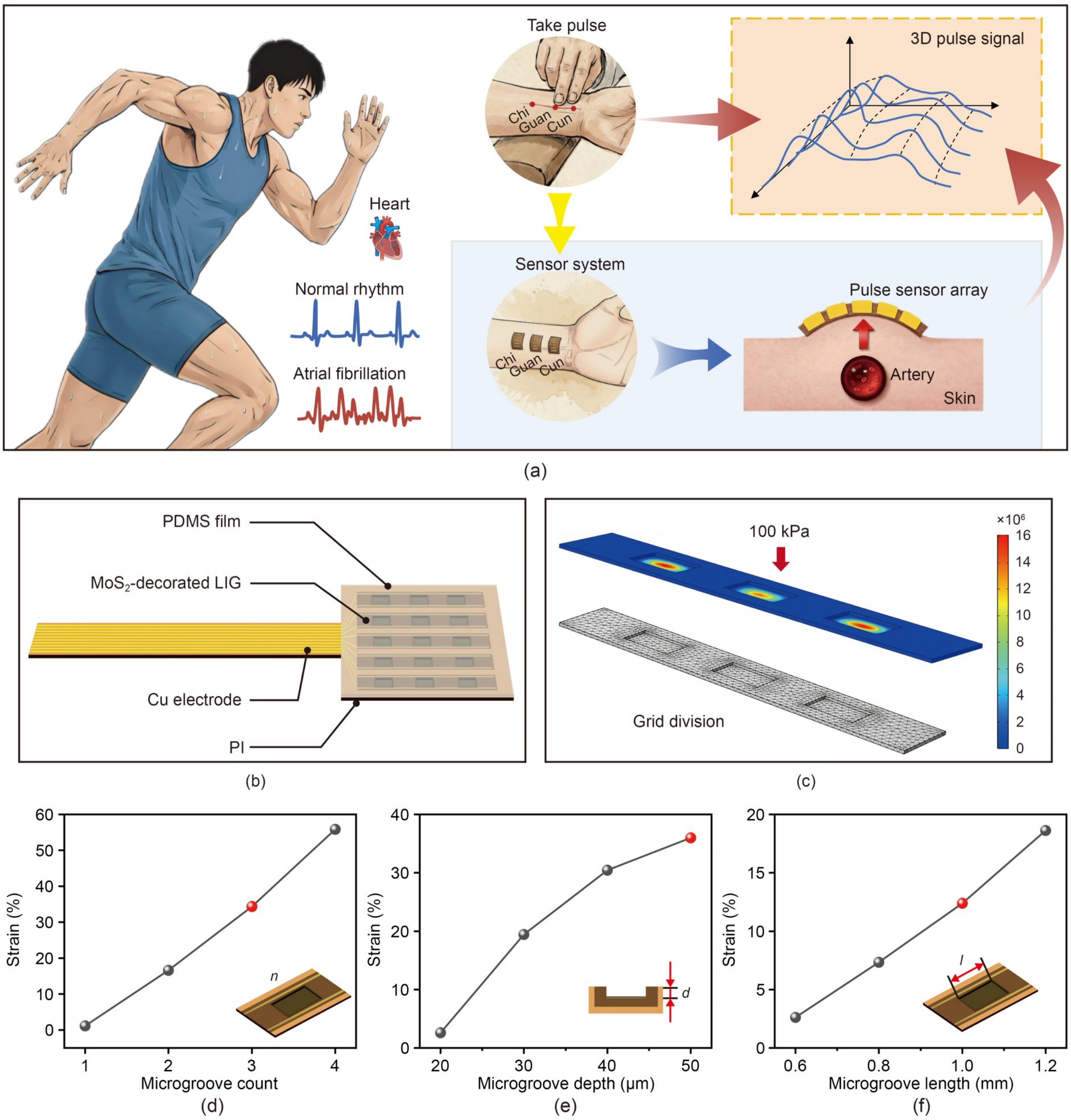

Fig. 1 Design of a 3D LIG sensor: (a) schematic of the sensor's operating mechanism; (b) exploded view layout; (c) in situ deformation within the LIG at 100 kPa (the legend is displacement, nm). FEA of the LIG yielded strain distributions for (d) varying numbers of microgrooves (*n*), (e) varying microgroove depths (*d*), and (f) varying microgroove lengths (*l*)

depth. However, the rate of strain increases gradually flattened as the depth increased. Furthermore, when the depth exceeded 50 μm, excessive undulations occurred during CO_2 laser focusing, adversely affecting the quality of the fabricated LIG. Therefore, a depth of 50 μm was chosen for the stress-concentrating structure. Finally, the influence of the stress concentrator length (*l*) was explored. As shown in Fig. 1f, increasing the length from 0.6 to 1.2 mm resulted in a rising strain level. Considering part constraints and manufacturing costs, a microgroove length of 1 mm was selected. Through the above finite element simulation analysis, the optimized microgroove structure parameters were determined to enhance the sensor sensitivity.

3.2 Fabrication process and characterization

The proposed sensor was fabricated using a mature preparation process. Fig. 2a illustrates the manufacturing process flow for the proposed pulse sensor array. After cutting PI to the designed dimensions, copper electrodes were fabricated via FPC ribbon cable technology to lead the output signals. Microgroove structures were fabricated on the PI film through precision machining, specifically milling, to create stress-concentrating features that enhance sensor sensitivity. Laser direct writing technology was employed to fabricate the LIG directly onto the PI surface across the microgrooves along the electrode lines. The laser etching technique eliminates the need for inert gases, making it suitable for large-scale batch production at low cost. Then, a MoS_2 solution was prepared, and the fabricated LIG@PI film was immersed into the solution. Ultrasonic agitation ensures MoS_2 modification of the LIG, guaranteeing consistency across different devices within the same batch. Finally, a chemical bonding encapsulation process was developed to assemble the PI film and a cover PDMS film at room temperature, effectively protecting the sensitive layer and enhancing device stability. Fig. 2b shows the as-prepared devices obtained via the above processes.

To fabricate microgrooves on the prepared PI substrates to enhance the sensitivity, a precision milling process was utilized due to its advantages of low cost, high efficiency, and high accuracy. The specific machining parameters for milling of microgrooves are summarized in Table S1 of the electronic supplementary materials (ESM), and the fabricated structures exhibit a high geometric fidelity relative to the initially designed parameters. Taking the depth of microgrooves as an example, the depth dimensions of five representative samples were characterized using a white-light interferometer (WLI). The results revealed a maximum depth deviation of only approximately 1 μm, with the average relative error across all samples measured at a remarkably low value of 1.12%, highlighting the high accuracy of precision milling. These results validate the promising application prospects of precision mechanical machining in the field of micro/nanosensors.

For the fabrication of LIG, the effects of laser power and scanning speed on the quality of graphene sensitive layers were investigated. The laser power directly correlates with the energy intensity; excessively high power may cause overablation, while insufficient power may prevent graphene formation. Experimentally, graphene edges exhibit significant defects under low thermal energy (<2.7 W), while high thermal energy (>3.3 W) causes severe carbonization of the PI film, resulting in loose and incomplete microstructures. As such, LIGs obtained at powers of 2.7, 3.0, and 3.3 W were selected for fabrication. Figs. S1a–S1c of the ESM display the LIG prepared at 2.7, 3.0, and 3.3 W, respectively, where the scanning speed was fixed at 100 mm/s. At 2.7 W, the graphene structure lacked a well-defined flake-like arrangement and exhibited loose, disordered packing. At 3.3 W, severe carbonization of graphene was clearly observed. The LIG prepared at 3.0 W exhibited the formation of uniform, flake-like microstructures without obvious defects or overablation. Additionally, the influence of the laser scanning speed was also investigated, as it could determine the interaction time between the laser and PI film. LIG morphologies were primarily observed at scanning speeds of 90, 100, and 110 mm/s under constant laser power of 3.0 W. Scanning speeds below 100 mm/s caused detachment of graphene flakes, while speeds exceeding 110 mm/s resulted in non-sheet-like graphene formation, as shown in Figs. S1d–S1f of the ESM. Based on the experimental results, an etching power of 3.0 W and a scanning speed of 100 mm/s were chosen for fabricating the final device. As shown in Fig. 2d, the LIG fabricated at 3.0 W and 100 mm/s exhibited a complete flake structure, with surface wrinkles and undulations to further increase its specific surface area.

The graphitization degree and elemental composition of LIG were also systematically investigated using Raman spectroscopy and XPS. The Raman spectrum in Fig. 2e exhibits three primary characteristic peaks: the D peak at about 1350 cm^{-1}, the G peak at about 1580 cm^{-1}, and the 2D peak at about 2700 cm^{-1}. The intensity ratio of the D peak to the G peak (I_D/I_G= 0.89) indicates a high degree of crystallization in the graphene formed within the LIG film. The relatively large ratio of the 2D peak to the G peak, coupled with the broad half-width of the 2D peak, suggests a distinct multilayer structure in the LIG (Zheng et al., 2023; Zou et al., 2023). Furthermore, the XPS spectrum (Fig. 2f) reveals that LIG was primarily composed of carbon (C), with trace amounts of oxygen (O) and nitrogen (N) elements. The C1s peak predominantly appears at approximately 285 eV, while the N1s peak appears at approximately 400 eV, and the O1s peak appears at approximately 532 eV. Overall, the C content significantly increases while the N and O contents

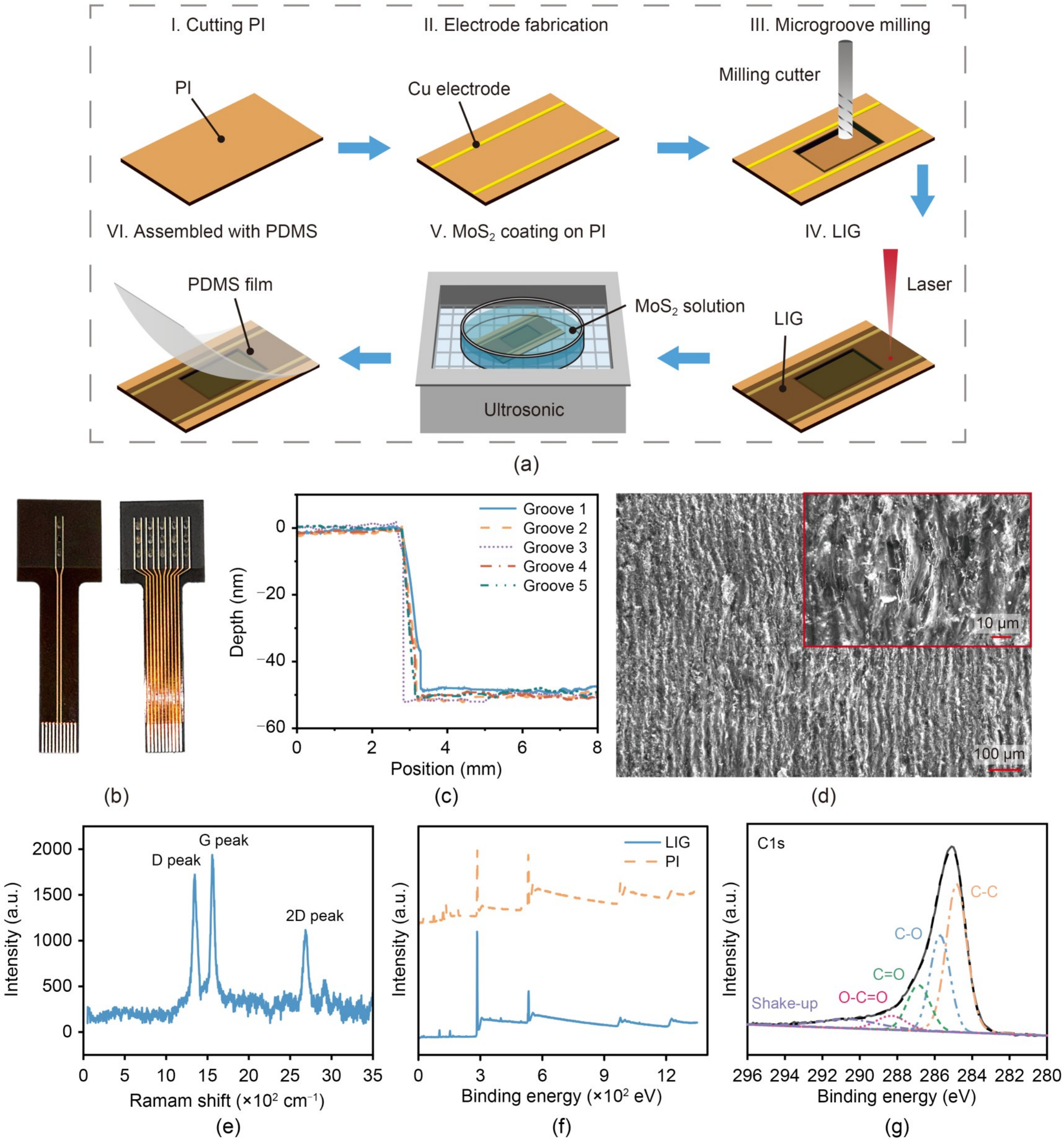

Fig. 2 Fabrication process and characterization of LIG pulse sensors: (a) fabrication process flow for the pulse sensor; (b) images of copper electrodes fabricated using the FPC ribbon process and a PI substrate with microgroove structures fabricated using the milling process; (c) schematic diagram showing the measurement of the depths of five microgrooves machined by the milling process; (d) SEM image and (e) Raman spectrum of porous graphene fabricated at a laser power of 3.0 W and a scanning speed of 100 mm/s; (f) comparative analysis of XPS spectra of the material before and after laser scanning; (g) XPS spectra of the LIG composite showing different deconvoluted peaks

markedly decrease after laser scribing, preliminarily confirming the successful conversion of PI into few-layer graphene. Analysis of the high-resolution XPS spectrum in the C1s region (Fig. 2g) reveals a peak at approximately 284.6 eV corresponding to sp^2-hybridized C-C bonds, a characteristic feature of graphene, indicating the presence of graphene materials.

MoS_2 shares a similar hexagonal structure with carbon atoms, as shown in Fig. S2 of the ESM, exhibiting a high Young's modulus and fracture strength. Unexpectedly and experimentally, it was found that incorporating MoS_2 modification into multilayer LIGs could mitigate graphene nanosheet fracture through the synergistic interaction between MoS_2's inherent active hierarchy and composite layers, thereby enhancing the consistency of the microstructural morphologies and, in turn, the electromechanical properties. After MoS_2 modification through dip-coating treatment, the morphology of MoS_2-decorated graphene was examined using SEM, as shown in Fig. S3 of the ESM. It could be clearly observed that MoS_2 nanosheets were embedded and bonded together with flaky graphene layers, reducing the dispersion of flaky structures and thereby enhancing structural consistency.

The encapsulation process is critical for ensuring stable and reliable sensor performance in practical applications. In particular, encapsulation of LIG not only shields the sensitive layer from external physical damage but also mitigates the adverse effects of ambient moisture on the LIG, thereby ensuring long-term functional stability. As such, a facile and novel bonding process between PI and PDMS at room temperature was developed. By employing MPTMS as an auxiliary material, efficient bonding between flexible plastic substrates and PDMS was achieved. Fig. S4 of the ESM illustrates the principle of the proposed chemical bonding process. Fig. S4a depicts a substrate bearing electrophilic groups, where δ^+ represents electrophilic sites and δ^- denotes nucleophilic sites. Fig. S4b illustrates the reaction process between the substrate and MPTMS aqueous solution: the alkoxy end of MPTMS undergoes hydrolysis, while its thiol functional group engages in a nucleophilic reaction with the substrate. The hydrolysis reaction of the MPTMS alkoxy end, which generates alcohol compounds and promotes cross-linking between adjacent MPTMS molecules, is shown in Fig. S4c. Fig. S4d illustrates the nucleophilic reaction between the MPTMS thiol group and the substrate, resulting in MPTMS grafting onto the substrate surface. The alkoxy-terminated silane-capped substrate formed after MPTMS modification is shown in Fig. S4e. Fig. S4f illustrates the oxidation reaction occurring on the surface of the PI substrate. Fig. S4g shows the dehydration reaction taking place at the conformal interface between the two substrates. The final product obtained after the bonding reaction is shown in Fig. S4h. The experimental procedure for this chemical bonding is illustrated in Fig. S5 of the ESM. First, the chemical modification of the PI surface using MPTMS was performed, followed by oxygen plasma treatment for both the PI substrate and the PDMS encapsulation structural layer. Finally, the two as-treated surfaces were precisely aligned and compressed, ultimately resulting in a permanent connection. To evaluate the shear and bonding strength, shear strength testing of the PI-PDMS assembly was conducted using a universal tensile testing machine, as depicted in Fig. S6 of the ESM. A shear bonding strength of approximately (312±25) kPa was recorded, accompanied by mechanical tearing between the PI substrate and PDMS cover, indicating reliable interfacial bonding.

3.3 Electromechanical performance

Experimental studies were conducted on the electromechanical performance of the sensor. Figs. 3a and 3b show response curves for sensors prepared with varying laser powers and scanning speeds, respectively. It is observed that relative current changes ($\Delta I/I_0$) increases with rising pressure, and the samples fabricated by 3.0 W laser power under constant scanning speed of 100 mm/s promise the highest sensitivity. Moreover, the response curves of sensors fabricated at different scanning speeds were also measured, in which the sensitivity also increased with the applied pressure. At a scanning speed of 100 mm/s, the sensitivity was significantly higher than those of other scanning speeds. The results further demonstrate that the morphology of the LIG sensing layer critically influences the sensing performance and the rationality of the selection of 3.0 W power and 100 mm/s for fabrication.

For the described LIG pressure sensor, we applied loads within the 0–180 kPa pressure range and reanalyzed the data for different pressure intervals using piecewise linear fitting. The slope of the fitted line obtained via the least squares method represents the sensitivity (S) of the sensor within the corresponding interval. As shown in Fig. 3c, a comparative analysis was conducted to examine the performance differences between sensors with and without microgroove structures. The experimental results indicate that with the introduction of microgroove structures, the sensor's S reached 2.205 kPa^{-1} in the low-pressure range (0–15 kPa) and 0.426 kPa^{-1} in the high-pressure range (15–180 kPa). In contrast, for the samples without microgrooves, the corresponding S values were 1.274 and 0.282 kPa^{-1}. This confirms that the increase in sensitivity aligns with the theoretical design: regions with abrupt geometric discontinuities exhibit significant stress concentration and are highly sensitive to local strain fluctuations. Furthermore, using the least-squares-fitted straight line in the figure as a baseline, the sensor's linearity was evaluated. After introducing the microgroove structure, the coefficient of determination (R^2)

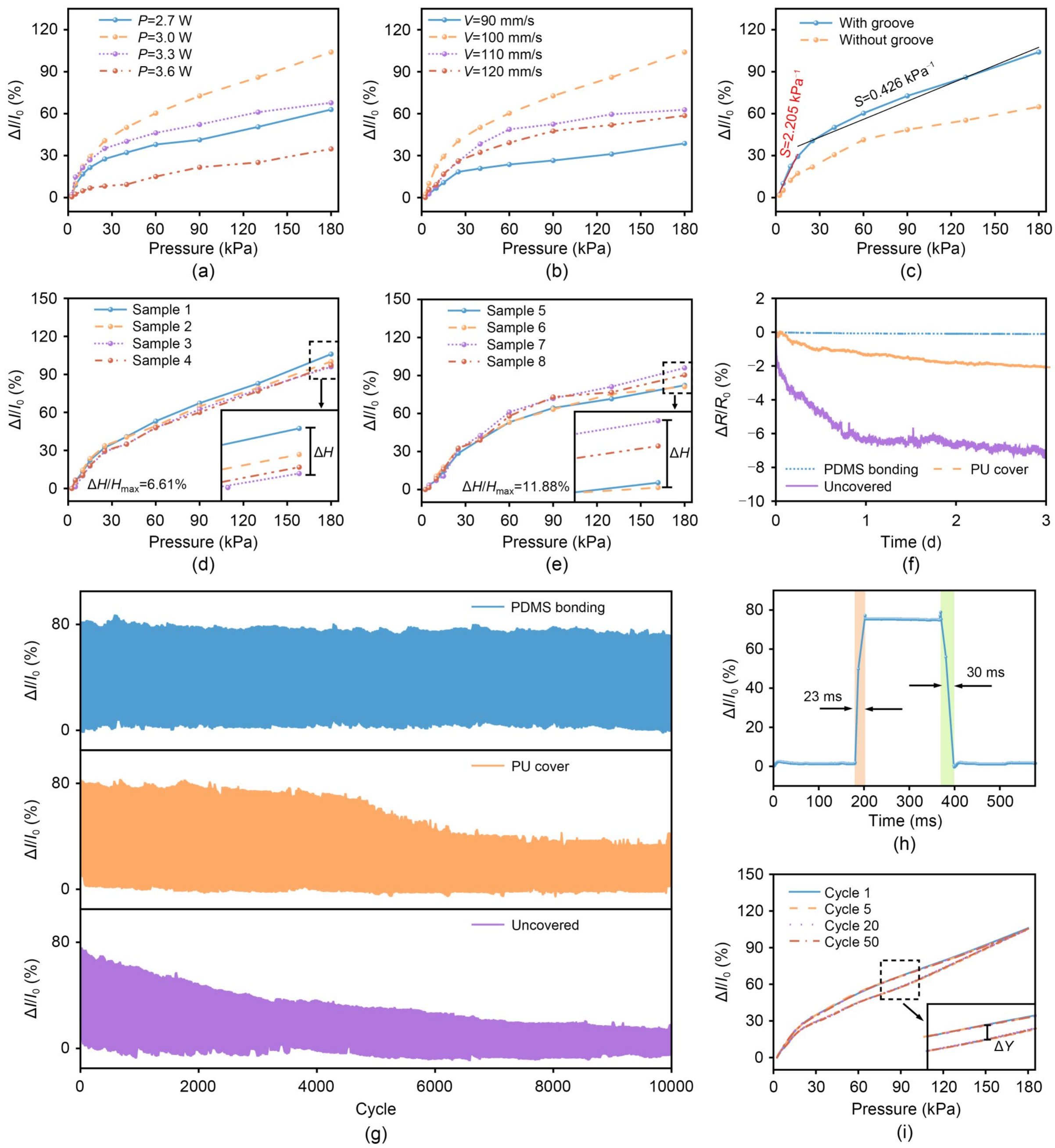

Fig. 3 Performance testing of the LIG pulse sensor: relative current variation of sensors fabricated at different (a) laser powers (*P*) and (b) scanning speeds (*V*) under pressures ranging from 0 to 180 kPa; (c) comparison of relative current changes at pressures ranging from 0 to 180 kPa for sensors with and without microgroove structures prepared at a laser power of 3.0 W and a scanning speed of 100 mm/s. Relative current changes ($\Delta I/I_0$) at different pressures for four sensors from the same batch: (d) with MoS_2 modification; (e) without MoS_2 modification; (f) initial resistance changes ($\Delta R/R_0$) over 3 d for three sensor types: uncovered, directly covered with PU film, and chemically bonded with PDMS; (g) relative current changes after over 10000 loading/unloading cycles for three sensor types: uncovered, directly covered with PU film, and chemically bonded with PDMS; (h) response time and recovery time of the sensor at 100 kPa; (i) changes (ΔY) in relative current and pressure during repeated loading and unloading cycles

in the low-pressure region (0–15 kPa) was 0.993, with a nonlinearity error (γ_L) of approximately 0.03%. In the high-pressure range (15–180 kPa), R^2 is 0.977, and γ_L is approximately 0.47%, indicating that the sensor exhibits excellent linear response characteristics. To evaluate the repeatability of the prepared sensors, comparative experiments were conducted on eight sensors, as shown in Figs. 3d and 3e. The results indicate that the maximum relative error ($\Delta H/H_{max}$, ΔH represents the maximum deviation in sensor characteristic curves, and H_{max} represents the full-scale output in sensor characteristic curves) between different devices was improved from 11.88% (Fig. 3e, without MoS_2 modification) to 6.61% (Fig. 3d, with MoS_2 modification). The results confirm that MoS_2 modification could significantly enhance the batch-to-batch consistency of the sensors, which is of paramount importance for practical applications. To evaluate the sensor's stability, initial resistance variations over three days were tested under ambient conditions in a naturally resting state. The tested sensors included samples without any encapsulation, samples simply covered with medical polyurethane (PU) tape, and samples covered with PDMS chemical bonding. As shown in Fig. 3f, the variations in the initial resistance under the three encapsulation conditions were approximately 7.44%, 2.15%, and 0.11%, confirming that PDMS bonding can effectively isolate LIG from atmospheric moisture, thereby mitigating the adverse effects of humidity on its sensing performance. Additionally, the three types of sensors were subjected to over 10000 mechanical load/unload cycles, and the results are recorded in Fig. 3g. The response curve of the unencapsulated sensor, directly exposed to air, gradually declined. The sensor encapsulated directly with medical PU tape exhibited a gradual performance degradation after 4000 cycles. In contrast, the sensor encapsulated with PDMS chemical bonding performs well, with the $\Delta I/I_0$ variation stabilizing within 0.01%, highlighting that the PDMS chemically bonded encapsulation could also lead to excellent stability over mechanical force. Table S2 provides a systematic comparison of this work with flexible pulse sensors reported in recent years.

Fig. 3h shows the sensor's response time and recovery time, which were approximately 23 and 30 ms under 100 kPa pressure, respectively, revealing the outstanding dynamic response performance of the as-prepared sensors. To evaluate the hysteresis characteristics of the sensors, Fig. 3i shows the mechanical response curves after the 1st, 5th, 20th, and 50th cycles, with a maximum hysteresis error (ΔY) of approximately 5.89%. The results indicate that the as-prepared sensor exhibits a relatively low hysteresis compared with other previously reported flexible pressure sensors (Wang and Tao, 2021; Wang et al., 2022). Furthermore, the sensor's response ability to mechanical loading under different frequencies was also investigated, as shown in Fig. S7 of the ESM. The sensor exhibited no frequency dependency within the 0–10 Hz range, making it suitable for common dynamic pressure sensing applications. Additionally, to meet the requirements for pulse monitoring, the sensor must possess the capability of subtle pressure detection. To determine the lower limit of detection, the sensors were subjected to a tiny force of 0.005 N (approximately 35 Pa), as shown in Fig. S8 of the ESM, and a distinct resistance change of 0.049% is discernible. Therefore, the sensor's minimum detectable force is determined to be approximately 35 Pa, which is sufficient for in-body pulse detection (Chou et al., 2022).

3.4 Applications

The developed LIG flexible pulse sensor was applied to human wrist pulse measurement using adhesive tape to conform to the curved surface of the radial artery skin at the target wrist location to acquire pulse signals. Fig. 4a displays an example of a single-point pulse signal acquired from a 20-year-old adult male at rest. Calculated from two consecutive systolic peaks, the arterial pulse rate is 74 beats per minute, with an interval of approximately 0.8 s. The inset figure shows a schematic diagram of the utilized sensor unit with only one sensing strip. Fig. 4b exhibits a detailed waveform of a selected pulse cycle extracted from Fig. 4a, comprising the pulse wave (P-wave, P_1 represents the amplitude of P-wave), tidal wave (T-wave, P_2 represents the amplitude of T-wave), double notch (D-notch), and double wave (D-wave). The time difference between the P-wave and T-wave (ΔT_{DVP}) was measured as approximately 233 ms, which falls within the normal range for healthy adult males in their twenties (Kang et al., 2016).

Beyond conventional single-point pulse monitoring, the defining highlight of this work lies in the sensor array design, which could enable comprehensive 3D pulse signal acquisition. To realize 3D pulse monitoring, a signal acquisition system was designed and constructed, as shown in Fig. 4c. The main control unit employs an ESP32 (ESPRESSIF SYSTEMS Co., Ltd., China) chip as microcontroller unit, utilizing its built-in analog-to-digital conversion (ADC) for data acquisition and transmitting data via a Wi-Fi module to a mobile application. Based on the as-prepared sensor array and signal acquisition system, pulse signal acquisition, processing, and display could be achieved, as depicted in Fig. 4d.

The monitoring system utilized three sensor arrays positioned at the subject's Cun (Sensor 1), Guan (Sensor 2), and Chi (Sensor 3) target sites. According to traditional Chinese pulse diagnosis theory, the Cun, Guan, and Chi acupoints are sequentially distributed along the radial artery, with Guan located at the most prominent pulsation region near the radial styloid process, Cun positioned toward the palm, and Chi toward the forearm. During the experiment, an experienced pulse diagnosis operator first identified the Guan region through digital palpation and subsequently determined the Cun and Chi positions using the traditional three-point positioning method. Three flexible sensor

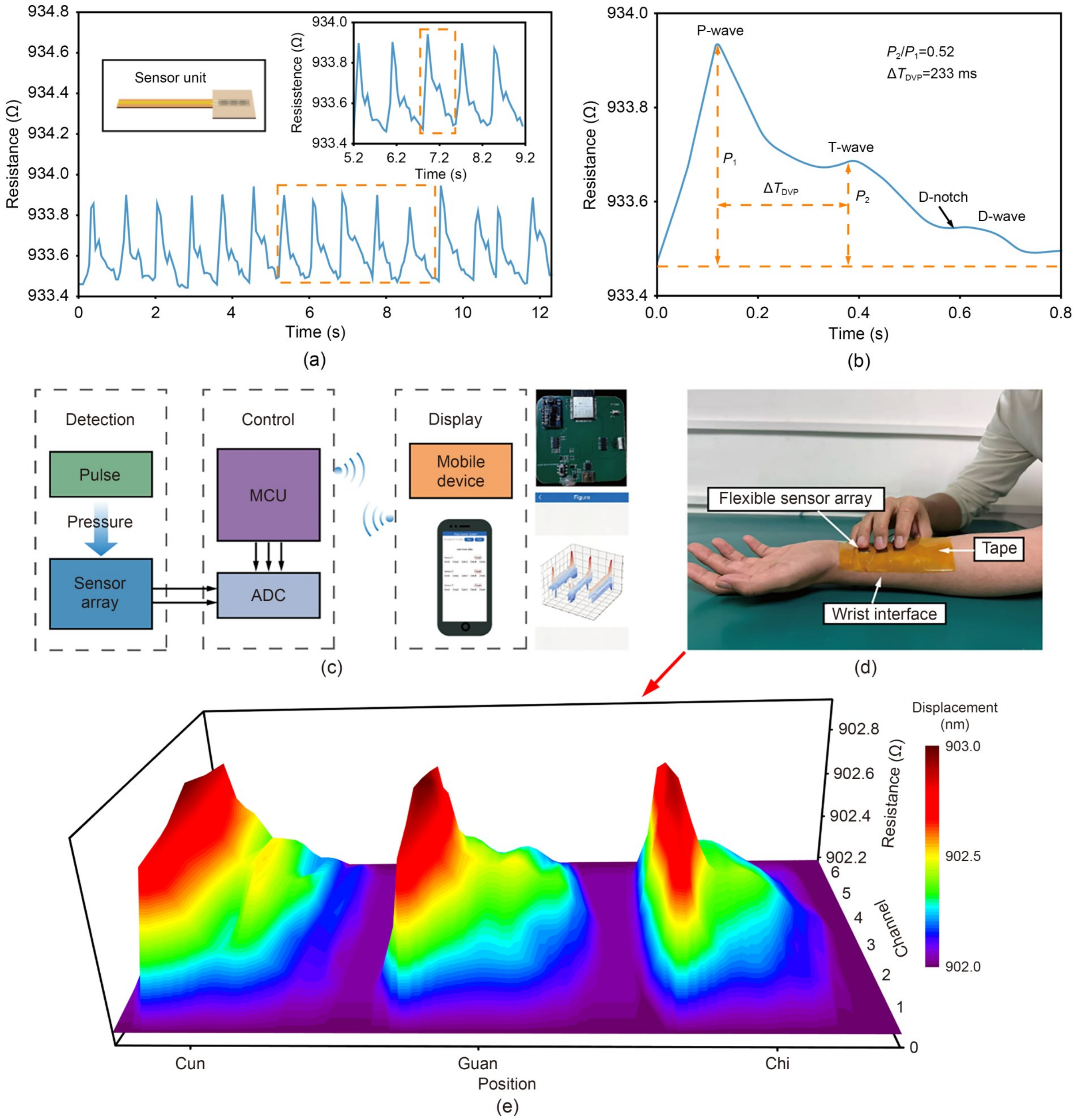

Fig. 4 Applications of the LIG pulse sensor: (a) real-time arterial pressure waveform measured by the sensor at the wrist (the inset shows an image of the sensor placed on the wrist and a local schematic of five cycles); (b) detailed image of the radial artery pulse wave during a single pulse cycle; (c) schematic diagram of the signal acquisition system (MCU: microcontroller unit; (d) 3D pulse signal acquisition process; (e) 3D pulse signal image of a single pulse cycle

arrays were then sequentially attached along the pulse pathway in the order of Cun–Guan–Chi, with an approximate center-to-center spacing of 12 mm between adjacent arrays. Owing to their intrinsic flexibility, the sensor arrays naturally conformed to the wrist surface and were secured using medical-grade hypoallergenic adhesive tape. To ensure stable skin contact while minimizing vascular compression, a light-touch adhesion strategy was adopted, and the static preload pressure was controlled below approximately 5 kPa. All measurements were performed with subjects in a relaxed seated posture, and all experiments were conducted by the same operator to ensure reproducibility, with sensor placement errors controlled within 5%.

Each flexible sensor array consisted of five independent LIG-sensitive units capable of synchronously acquiring pulse signals from different spatial positions at a single acupoint. After signal acquisition, the raw electrical data from each channel were filtered and normalized to suppress environmental noise. The spatial coordinates of the five sensing units, together with their corresponding real-time response amplitudes, were subsequently used to reconstruct the local 2D pulse distribution. By further incorporating continuous temporal sequence data through interpolation and surface fitting, a dynamic 3D pulse image describing the "spatial location–time–response amplitude" relationship was generated to visualize pulse wave propagation characteristics. Notably, the reconstructed "3D pulse signal" in this study represents a spatiotemporal visualization of multichannel pulse responses rather than a strict 3D biomechanical pressure field reconstruction. Fig. S10 of the ESM illustrates the workflow for processing and reconstructing 3D pulse sensor data. Fig. 4e shows the final 3D pulse image of an adult male at rest, clearly reflecting the propagation process of the pulse signal. All measurement target sites exhibited stable, periodic pulse waveforms with distinct peaks, indicating that the sensor is capable of effectively capturing the dynamic changes in the human pulse. The constructed 3D pulse images not only provide a visual representation of the temporal evolution of the pulse signal but also reveal its spatial distribution patterns, which are suitable for analyzing the health information of the subject. Overall, our LIG flexible pulse sensor serves as a versatile skin-interface pulse sensor capable of long-term stable monitoring of cardiovascular status.

4 Conclusions

In summary, a design and fabrication method for highly sensitive and robust LIG flexible pulse sensor arrays has been developed. First, a precision machining process was employed to mill microgroove structures on the PI substrate before fabrication of LIG, achieving sensitivity enhancement through the stress concentration effect. Then, the microstructural consistency of the LIG was improved via MoS_2 solution modification, thereby enhancing the uniformity of the electromechanical response. Finally, a facile and reliable chemical bonding technique was developed to isolate the LIG from atmospheric moisture, simultaneously enhancing the stability of the sensor's electromechanical response. Consequently, the as-prepared sensor exhibited outstanding performance, such as high sensitivity, good consistency, fast response capability, and excellent stability. Leveraging these advantages, the fabricated sensor arrays have been successfully applied in detecting 3D pulse signals. This work offers an effective strategy to address the limitations of traditional pulse sensors, promising the potential future applications of this flexible pulse sensor technology in the fields of health monitoring and smart healthcare.

In addition, further research is needed in the following areas. First, this study is currently still in the proof-of-concept stage, with a relatively limited number of participants. Systematic testing involving large-scale populations across multiple age groups and under various physiological conditions has not yet been conducted, and further research is needed. Second, because multiple sensing units are integrated onto the same flexible substrate, a certain degree of signal crosstalk is inevitable during actual data acquisition. In future work, we plan to further reduce crosstalk between adjacent units by employing isolation structures such as lead bridges and serpentine beam structures.

Acknowledgments

This work is supported by the National Natural Science Foundation of China (No. 52405626) and the S&T Program of Energy Shaanxi Laboratory (No. ESLB202436), China.

Author contributions

Guoxi LUO designed the research and wrote the first draft of the manuscript. Diying PI performed the experiments. Wenyan LI and Ping YANG processed the corresponding data. Ryutaro MAEDA and Zhuangde JIANG helped to provide suggestions and organize the manuscript. Min LI and Libo ZHAO supervised the project and provided funding.

Conflict of interest

Guoxi LUO, Diying PI, Wenyan LI, Min LI, Ping YANG, Ryutaro MAEDA, Libo ZHAO, and Zhuangde JIANG declare that they have no known competing financial interests or personal relationships that could have appeared to influence the work reported in this paper.

Declaration on the use of generative AI tools

All contributions from generative AI are transparently disclosed, and no AI tool has been used to fabricate data, plagiarise existing literature or evade academic writing norms.

Data availability

The data that support the findings of this study are available from the corresponding author upon reasonable request.

References

Ali M, Hoseyni SM, Das R, et al., 2023. A flexible and biodegradable piezoelectric-based wearable sensor for non-invasive monitoring of dynamic human motions and physiological signals. *Advanced Materials Technologies*, 8(15): 2300347.
https://doi.org/10.1002/admt.202300347

Cao YJ, Li P, Zhu YR, et al., 2025. Artificial intelligence-enabled novel atrial fibrillation diagnosis system using 3D pulse perception flexible pressure sensor array. *ACS Sensors*, 10(1):272-282.
https://doi.org/10.1021/acssensors.4c02395

Chen JZ, Sun K, Zheng R, et al., 2021. Three-dimensional arterial pulse signal acquisition in time domain using flexible pressure-sensor dense arrays. *Micromachines*, 12(5):569.
https://doi.org/10.3390/mi12050569

Chhetry A, Sharifuzzaman M, Yoon H, et al., 2019. MoS_2-decorated laser-induced graphene for a highly sensitive, hysteresis-free, and reliable piezoresistive strain sensor. *ACS Applied Materials & Interfaces*, 11(25):22531-22542.
https://doi.org/10.1021/acsami.9b04915

Chou CH, Yin JH, Lin YK, et al., 2022. The optimal pulse pressures for healthy adults with different ages and sexes correlate with cardiovascular health metrics. *Frontiers in Cardiovascular Medicine*, 9:930443.
https://doi.org/10.3389/fcvm.2022.930443

Chowdhury AH, Jafarizadeh B, Baboukani AR, et al., 2023. Monitoring and analysis of cardiovascular pulse waveforms using flexible capacitive and piezoresistive pressure sensors and machine learning perspective. *Biosensors and Bioelectronics*, 237:115449.
https://doi.org/10.1016/j.bios.2023.115449

Diana G, Scardulla F, Puleo S, et al., 2025. Non-invasive estimation of arterial stiffness using photoplethysmography sensors: an in vitro approach. *Sensors*, 25(11):3301.
https://doi.org/10.3390/s25113301

Fei XX, Huang JY, Shi WQ, 2023. Humidity sensor composed of laser-induced graphene electrode and graphene oxide for monitoring respiration and skin moisture. *Sensors*, 23(15): 6784.
https://doi.org/10.3390/s23156784

Gao TT, Qiu XL, Xu P, et al., 2025. Piezoelectret-based dual-mode flexible pressure sensor for accurate wrist pulse signal acquisition in health monitoring. *Measurement*, 242: 116283.
https://doi.org/10.1016/j.measurement.2024.116283

Guan YF, Li Y, Zheng Y, et al., 2025. Fabrication of an on-demand removable glucose sensor patch based on laser-induced graphitization technology for sweat monitoring in individuals with fragile skin. *Microchimica Acta*, 192(12): 846.
https://doi.org/10.1007/s00604-025-07675-z

Hou YY, Xie HB, Li YB, et al., 2025. A laser-induced wide-range thin-film temperature sensor without additional anti-oxidative encapsulations. *International Journal of Extreme Manufacturing*, 7(6):065508.
https://doi.org/10.1088/2631-7990/adefa2

Huang QL, Dai XM, Guo S, et al., 2024. Flexible, wearable and sensitive laser-induced graphene sensors for human health monitoring. *Polymers for Advanced Technologies*, 35(6):e6473.
https://doi.org/10.1002/pat.6473

Kang SB, Lee J, Lee S, et al., 2016. Highly sensitive pressure sensor based on bioinspired porous structure for real-time tactile sensing. *Advanced Electronic Materials*, 2(12): 1600356.
https://doi.org/10.1002/aelm.201600356

Kang XX, Huang L, Zhang YT, et al., 2023. Wearable multi-channel pulse signal acquisition system based on flexible MEMS sensor arrays with TSV structure. *Biomimetics*, 8(2):207.
https://doi.org/10.3390/biomimetics8020207

Li X, Liang Q, Liu HF, et al., 2025. High-sensitivity MXene/MWCNTs/PDMS flexible capacitive sensor for wearable health monitoring. *Advanced Materials Technologies*, 10(18):e00677.
https://doi.org/10.1002/admt.202500677

Li YM, Lu J, Zhou YY, et al., 2025. Electret-based wrist-worn pressure sensor for non-invasive monitoring of pulse and blood pressure. *Cell Reports Physical Science*, 6(11): 102914.
https://doi.org/10.1016/j.Xcrp.2025.102914

Lin J, Peng ZW, Liu YY, et al., 2014. Laser-induced porous graphene films from commercial polymers. *Nature Communications*, 5:5714.
https://doi.org/10.1038/ncomms6714

Liu CX, Ma F, Sun QC, et al., 2024. Highly sensitive flexible capacitive pressure sensor based on a multicross-linked dual-network ionic hydrogel for blood pressure monitoring applications. *ACS Applied Materials & Interfaces*, 16(26):

34042-34056.
https://doi.org/10.1021/acsami.4c04686

Liu SY, Lu SQ, Zheng XY, et al., 2025. Laser-induced graphene/ITO heterostructure for self-powered ion sensing via ionovoltaic effect. *Chemical Engineering Journal*, 525:170252.
https://doi.org/10.1016/j.Cej.2025.170252

Lu YY, Jin ZG, Jian YH, et al., 2025. Metal–hydrogel chelation interfaces for ultrasoft and bidirectional bioelectronics. *National Science Review*, 12(11):nwaf399.
https://doi.org/10.1093/nsr/nwaf399

Lu YY, Jin ZG, Sheng QC, et al., 2026. Universal modulus-free transfer of scalable laser-induced graphene for electronic skins. *Nature Communications*, 17(1):1381.
https://doi.org/10.1038/s41467-025-68131-3

Luo GX, Zhang BC, Pi DY, et al., 2025. Chemically bonded flexible pressure sensor based on divergent metallic grid with high linearity, low hysteresis, and excellent stability. *Sensors and Actuators A: Physical*, 392:116670.
https://doi.org/10.1016/j.sna.2025.116670

Luo HY, Cai ZM, Yang G, et al., 2026. Laser-programmed stiffness and interfaces for textile hybrid electronics. *Nature Communications*, 17(1):357.
https://doi.org/10.1038/s41467-025-67149-x

Mu M, Chen GM, Yu WJ, et al., 2024. In situ growth of laser-induced graphene on flexible substrates for wearable sensors. *ACS Applied Nano Materials*, 7(3):3279-3288.
https://doi.org/10.1021/acsanm.3c05669

Pang Y, Zhang KN, Yang Z, et al., 2018. Epidermis microstructure inspired graphene pressure sensor with random distributed spinosum for high sensitivity and large linearity. *ACS Nano*, 12(3):2346-2354.
https://doi.org/10.1021/acsnano.7b07613

Raza T, Tufail MK, Ali A, et al., 2022. Wearable and flexible multifunctional sensor based on laser-induced graphene for the sports monitoring system. *ACS Applied Materials & Interfaces*, 14(48):54170-54181.
https://doi.org/10.1021/acsami.2c14847

Sultana R, Ang FJL, Lim SL, et al., 2026. Measurement properties of English and Chinese versions of HeartQoL in a multiethnic Asian cohort with cardiovascular disease. *Value in Health Regional Issues*, 54:101554.
https://doi.org/10.1016/j.vhri.2025.101554

Tian G, Deng WL, Yang T, et al., 2024. Hierarchical piezoelectric composites for noninvasive continuous cardiovascular monitoring. *Advanced Materials*, 36(26):2313612.
https://doi.org/10.1002/adma.202313612

van Steijn NJ, Pepplinkhuizen S, Postema PG, et al., 2025. Ventricular arrhythmia detection with a wearable ring-type photoplethysmography sensor: a feasibility study. *Heart Rhythm*, 22(12):3082-3089.
https://doi.org/10.1016/j.Hrthm.2025.06.008

van Volkenburg T, Ayoub D, Alemán Reyes A, et al., 2023. Practical considerations for laser-induced graphene pressure sensors used in marine applications. *Sensors*, 23(22):9044.
https://doi.org/10.3390/s23229044

Vojnović V, Spasenović M, Pešić I, et al., 2025. Pulse sensors based on laser-induced graphene transferred to biocompatible polyurethane networks: fabrication, transfer methods, characterization, and application. *Chemosensors*, 13(4):122.
https://doi.org/10.3390/chemosensors13040122

Wang F, Tao XM, 2021. Carbon/silicone nanocomposite-enabled soft pressure sensors with a liquid-filled cell structure design for low pressure measurement. *Sensors*, 21(14):4732.
https://doi.org/10.3390/s21144732

Wang WT, Deng ZP, Chen ZQ, et al., 2025. Laser-induced and conformal liquid-silicone casting of oxalis-inspired graphene-based piezoresistive pressure sensors. *Journal of Bionic Engineering*, 22(2):713-726.
https://doi.org/10.1007/s42235-024-00644-x

Wang XJ, Li H, Wang TY, et al., 2022. Flexible and high-performance piezoresistive strain sensors based on multi-walled carbon nanotubes@polyurethane foam. *RSC Advances*, 12(22):14190-14196.
https://doi.org/10.1039/d2ra01291j

Wu YF, Li YL, Wang X, et al., 2025. Intelligent ring for dynamic pulse wave monitoring using fine tubular triboelectric nanogenerators. *Nano Energy*, 134:110581.
https://doi.org/10.1016/j.Nanoen.2024.110581

Xing XQ, Zou Y, Zhong M, et al., 2024. A flexible wearable sensor based on laser-induced graphene for high-precision fine motion capture for pilots. *Sensors*, 24(4):1349.
https://doi.org/10.3390/s24041349

Xu ZY, Wang ZH, Wang J, et al., 2025. A multi-indicator pulse monitoring system based on an ultra-sensitive and stable self-powered wearable triboelectric sensor with assistance of personalized deep learning. *Nano Energy*, 140:111039.
https://doi.org/10.1016/j.nanoen.2025.111039

Yang G, Tian MZ, Huang P, et al., 2021. Flexible pressure sensor with a tunable pressure-detecting range for various human motions. *Carbon*, 173:736-743.
https://doi.org/10.1016/j.carbon.2020.11.066

Yang QQ, Li BQ, Wang MK, et al., 2025. Machine learning-enhanced modular ionic skin for broad-spectrum multimodal discriminability in bidirectional human–robot interaction. *Advanced Materials*, 37(42):e08795.
https://doi.org/10.1002/adma.202508795

Yang XC, Chen WZ, Fan QF, et al., 2024. Electronic skin for health monitoring systems: properties, functions, and applications. *Advanced Materials*, 36(31):2402542.
https://doi.org/10.1002/adma.202402542

Zhang R, Lin J, He T, et al., 2024. High-performance piezoresistive sensors based on transfer-free large-area $PdSe_2$ films for human motion and health care monitoring. *InfoMat*, 6(1):e12484.
https://doi.org/10.1002/inf2.12484

Zhang XK, Chai J, Xu LX, et al., 2025. Direct extraction of respiratory information from pulse waves using a finger-inspired

flexible pressure sensor system. *Microsystems & Nanoengineering*, 11(1):90.
https://doi.org/10.1038/s41378-025-00924-4

Zhao J, Luo JS, Zhou ZW, et al., 2021. Novel multi-walled carbon nanotubes-embedded laser-induced graphene in crosslinked architecture for highly responsive asymmetric pressure sensor. *Sensors and Actuators A: Physical*, 323: 112658.
https://doi.org/10.1016/j.sna.2021.112658

Zheng CY, Wang X, Gu RQ, et al., 2025. The burden of cardiovascular disease in China: incidence estimates from national surveillance (2023). *JACC*, 87(12):1453-1465.
https://doi.org/10.1016/j.jacc.2025.08.060

Zheng HH, Wang H, Yi KR, et al., 2023. Wearable LIG flexible stress sensor based on spider web bionic structure. *Coatings*, 13(1):155.
https://doi.org/10.3390/coatings13010155

Zou Y, Zhong M, Li SC, et al., 2023. Flexible wearable strain sensors based on laser-induced graphene for monitoring human physiological signals. *Polymers*, 15(17):3553.
https://doi.org/10.3390/polym15173553

Electronic supplementary materials

Tables S1 and S2, Figs. S1–S10